Bio-inspired ultra-thin microfluidics for soft sweat-activated batteries and skin electronics

Mengge Wu [a,b,‡], Rui Shi [b,‡], Jingkun Zhou [b,c‡], Tsz Hung Wong [b], Kuanming Yao [b], Jian Li [b,c], Xingcan Huang [b], Dengfeng Li [b,c], Yuyu Gao [b], Yiming Liu [b], Sihui Hou [a, b], Junsheng Yu [a*], Xinge Yu [b,c,d*]

[a] State Key Laboratory of Electronic Thin Films and Integrated Devices, School of Optoelectronic Science and Engineering, University of Electronic Science and Technology of China (UESTC), Chengdu 610054, China. Email: jsyu@uestc.edu.cn

[b] Department of Biomedical Engineering, City University of Hong Kong, Hong Kong, China. Email: xingeyu@cityu.edu.hk

[c] Hong Kong Center for Cerebra-Cardiovascular Health Engineering, Hong Kong Science Park, New Territories, Hong Kong, China

[d] Shenzhen Research Institute City University of Hong Kong, Shenzhen 518057, China

‡ M. Wu, R. Shi and J. Zhou contributed equally to this work.

Table S1 The typical reported flexible aqueous batteries.

Anode	Cathode	Salt bridge	Power density	Open-circuit voltage (V)	Discharge capacity	Ref.
Zn	Ag_2O	KOH/LiOH	/	1.31	2.5 mA·h/cm^2	1
Al	Ag_2O	H_2O	26.6 μW·h cm^{-2} μm^{-1}	1.75	7.17 μA·h	2
Zn	pyrrole - Carbon Nanotubes	protein	60 μA/cm^2	~ 0.9	/	3
Mg	Ag/AgCl	NaCl	/	~ 1.6	67 A·h·Kg	4
Mg	Ag	H_2O	3.0 mW/cm^2	2.2	/	5
Mg	O_2	KCl	16.3 mW/cm^2	1.41	74.7 mA·h	6
Zn	Cu	KCl	7.46 mW/cm^2	0.93	42.5 mA·h	7
Mg	Ag_2O/graphene	KCl	122 mW/cm^2	1.91	8.33 mA·h	This work

References:

1. R. Kumar, J. Shin, L. Yin, J. M. You, Y. S. Meng and J. Wang, *Advanced Energy Materials*, 2017, **7**, 1602096.
2. E. F. Garay and R. Bashirullah, *Journal of Microelectromechanical Systems*, 2014, **24**, 70-79.
3. S. Li, Z. P. Guo, C. Y. Wang, G. G. Wallace and H. K. Liu, *Journal of Materials Chemistry A*, 2013, **1**, 14300-14305.
4. A. Bandodkar, S. Lee, I. Huang, W. Li, S. Wang, C.-J. Su, W. Jeang, T. Hang, S. Mehta and N. Nyberg, *Nature Electronics*, 2020, **3**, 554-562.
5. Y. Koo, J. Sankar and Y. Yun, *Biomicrofluidics*, 2014, **8**, 054104.
6. Y. Liu, X. Huang, J. Zhou, J. Li, S. K. Nejad, C. K. Yiu, H. Li, T. H. Wong, W. Park and K. Yao, *Nano Energy*, 2022, **92**, 106755.
7. Y. Liu, X. Huang, J. Zhou, C. K. Yiu, Z. Song, W. Huang, S. K. Nejad, H. Li, T. H. Wong and K. Yao, *Advanced Science*, 2104635.

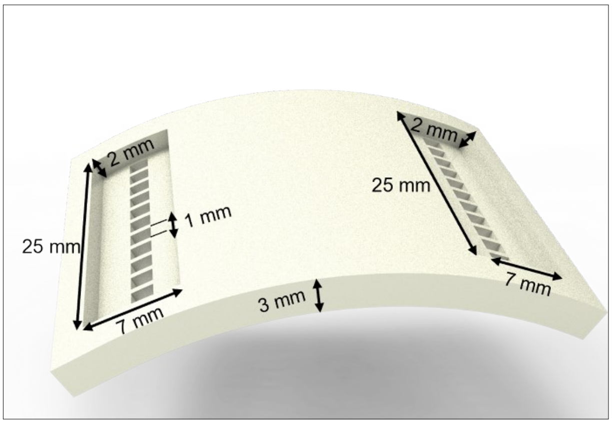

Fig. S1 Design details of PDMS encapsulation cap.

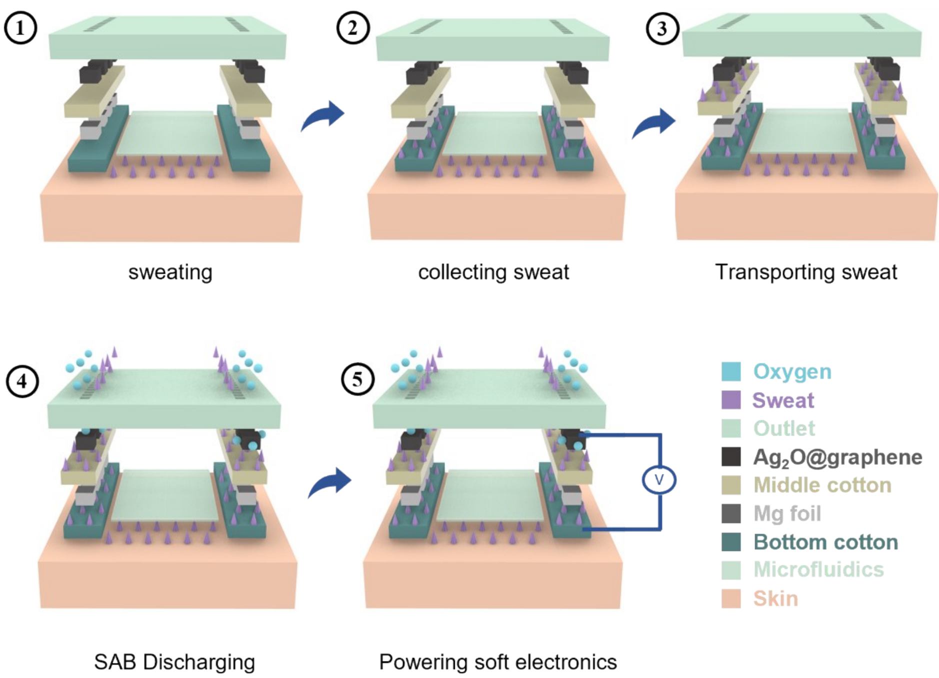

Fig. S2 Working mechanism of the SAB platform. (1) Sweating on the skin surface, (2) Sweat is collected by microfluidics into the bottom cotton layer, (3) Sweat transports to the middle cotton layer, (4) The battery is activated and discharged, (5) The battery platform supplies power to the external soft electronics.

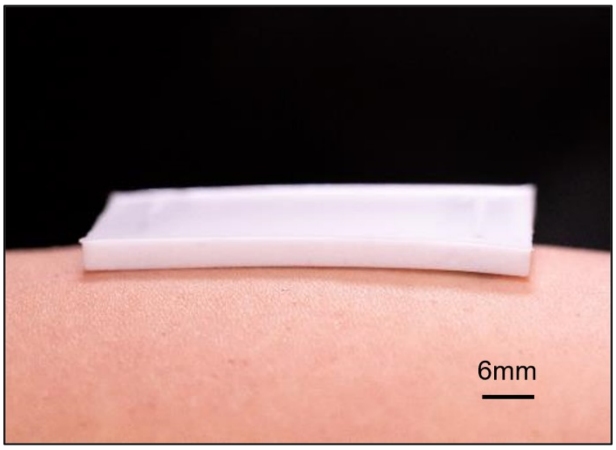

Fig. S3 The photography of SAB platform mounted on the volunteer's wrist in the side view, demonstrating an intimate adaptation.

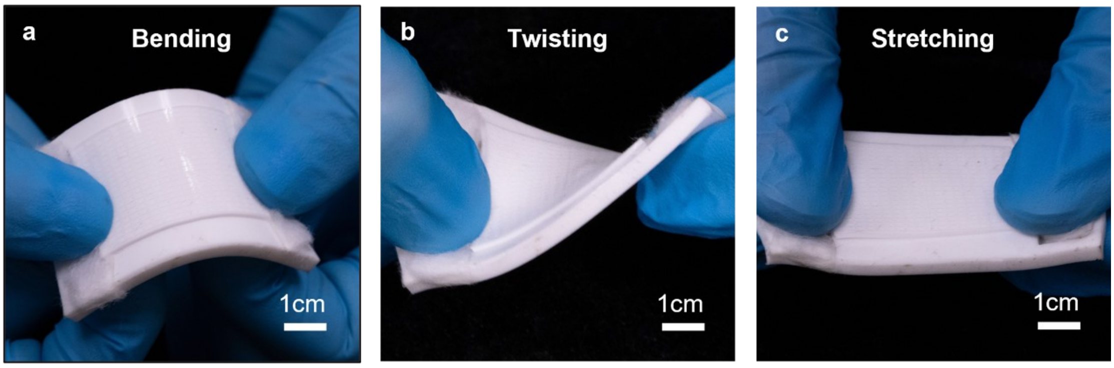

Fig. S4 The photographs of SAB platform in states of (a) bending, (b) twisting and (c) stretching, illustrating a great mechanical flexibility of SAB platform that can adapt to the deformation caused by various human motions.

Table S2 The absorption capability of the middle cotton layer in SABs based on microfluidics.

Water added in microfluidics (μL)	**Water absorbed by bottom cotton layer (μL)**	**Wetness of bottom cotton layer**	**Wetness of middle cotton layer**	**SAB cell activated**
10	1.15	slightly	slightly	No
20	4.50	moderately	slightly	Yes
30	7.95	moderately	half	Yes
50	15.25	moderately	significantly	Yes
100	29.75	half	almost	Yes
150	40.50	significantly	almost	Yes
200	45.00	almost	almost	Yes
250	49.95	almost	almost	Yes
300	62.20	almost	almost	Yes
350	74.10	almost	almost	Yes
400	85.00	almost	almost	Yes

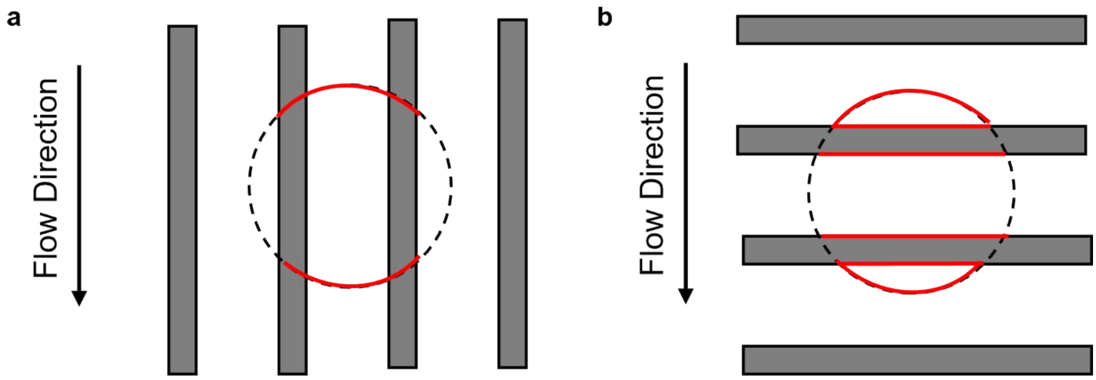

Fig. S5 Schematic illustration of three-phase contact line (TCL) of a water droplet in the parallel microgrooves spreading along (a) the longitudinal direction and (b) the transverse direction. (White, microgrooves; gray, walls; circle, boundary of the water droplet; red line, effective TCLs which affect the spreading behavior)

Note 1. Liquid movement along the microgrooves

As for hydrophilic microgroove arrays, the surface adhesion is determined by the contact areas with the bottom and walls of microgrooves. When liquid moves along with the longitudinal direction, the motion of TCL is continuous (**Fig. S5(a)**). However, the liquid needs to step across the next microgroove one by one in the transverse spreading process. The longer and discontinuous TCL leads to a higher energy barrier (**Fig. S5(b)**). What's more, the walls of the microgrooves, several hundred micrometers thick, are another obstacle to the transverse spread of the liquid.

Note 2. Liquid movement along the interconnected sawtooth-shaped capillary channels

When a liquid is applied to the above structure, it forms a meniscus at each free liquid–air interface due to the surface tension. The passive liquid transport relies on the positive capillary driving pressure difference ΔP between the interfaces, which describes by the Young-Laplace equation:

$$\Delta P = \gamma(\frac{1}{r_1} + \frac{1}{r_2}),$$

where r_1 and r_2 are the principal radii of curvature of the liquid meniscus, and γ is the surface tension. The curvature of the meniscus can be either concave or convex, depending on the contact angle θ, which results in a positive or negative radius of curvature, respectively. Therefore, a positive ΔP leads to passive liquid transport, while a negative ΔP results in halting of the liquid.

When a liquid is transported along with the structure by capillary forces, the advancing front of the liquid first stops at the abrupt widening edge with infinite meniscus radius (capillary I), but further enters the narrower channel (capillary II). If the liquid front in capillary II reaches a nearby interconnect, it will in turn be delivered to capillary I. The liquid halting in capillary I is picked up by the liquid at the interconnection, forming a new meniscus. After that, the liquid is transported through a second interconnection into capillary II, where the stopped liquid is picked up. The narrowing channels favour water transport due to the curvature of the liquid-air interface. The lateral interconnecting channels overcome the effects of the abrupt widening and help maintain an advancing liquid front. However, in the backward direction, liquid stops at the widening channels, and there is no interconnection to pick up the halted liquid front.

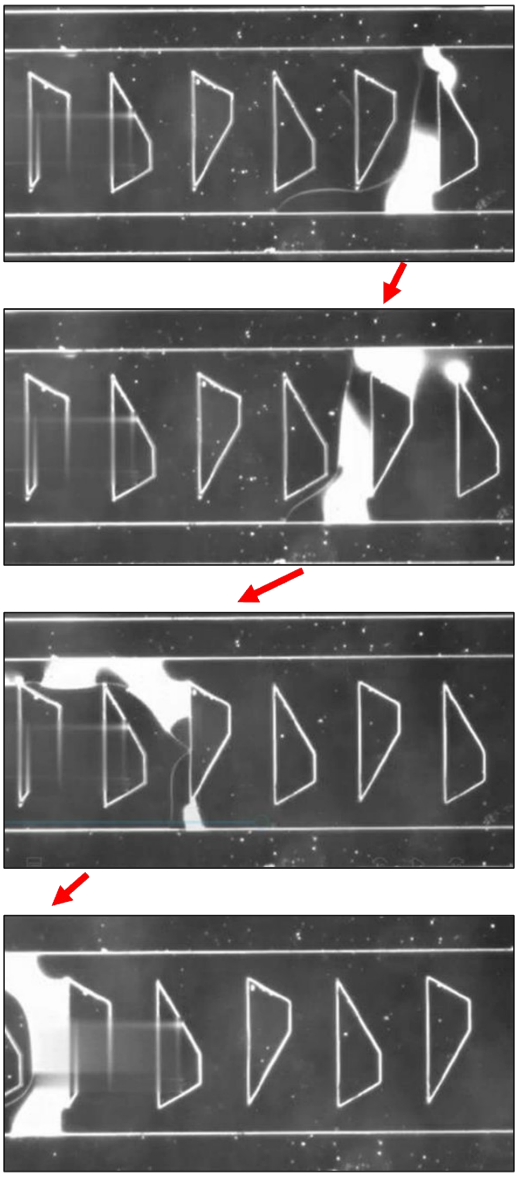

Fig. S6 Optical images to illustrate the drainage function of the bio-inspired microfluidic system.

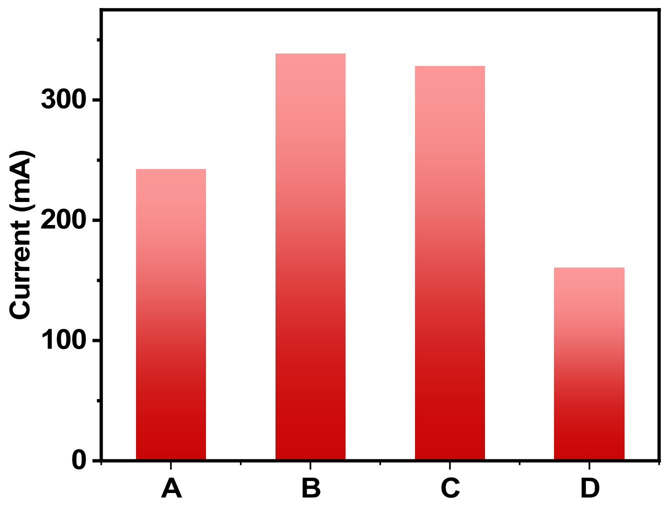

Fig. S7 Short-circuit current of SAB with different anodes that a 5-ohm resistor was connected in series in the circuit. A-D refer to the SABs based on the anodes of pure graphene, Ag_2O: graphene=1: 1, Ag_2O: graphene=2: 1, and pure conductive carbon cloth.

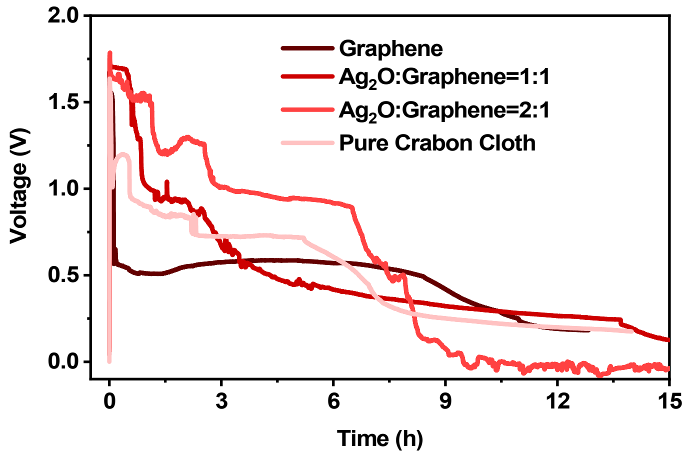

Fig. S8 Open-circuit voltage of SAB with different anode.

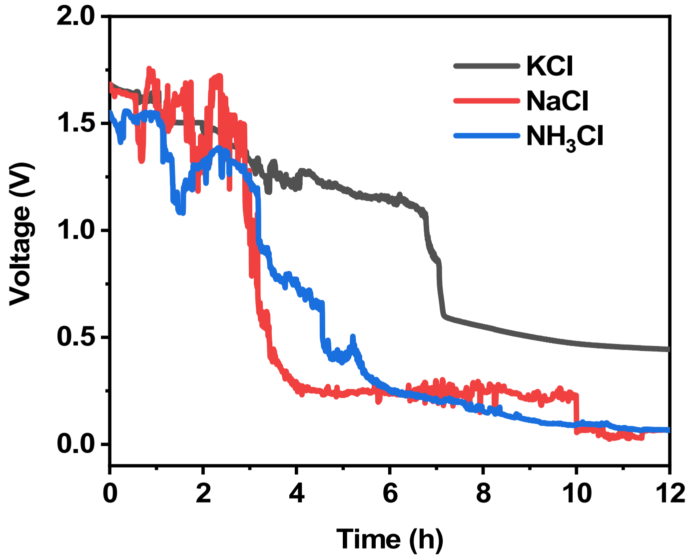

Fig. S9 Open-circuit voltage of SABs with different salt bridges.

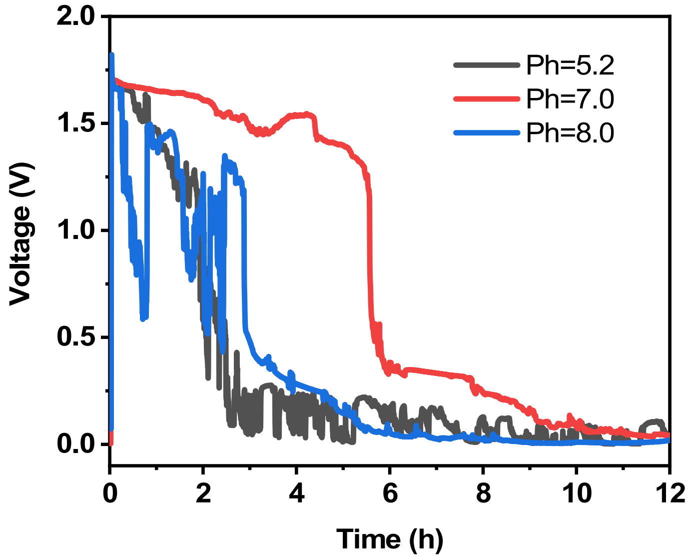

Fig. S10 Open-circuit voltage of SABs with KCl solution in different pH values.

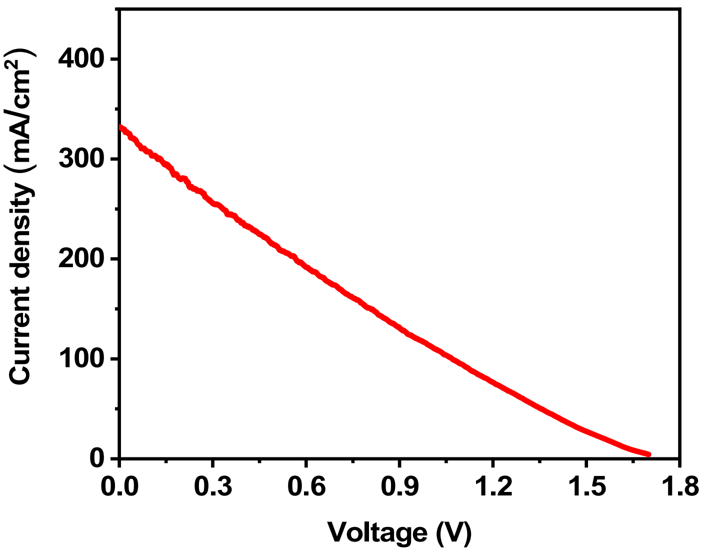

Fig. S11 Current density generated by the SAB as a function of voltage output.

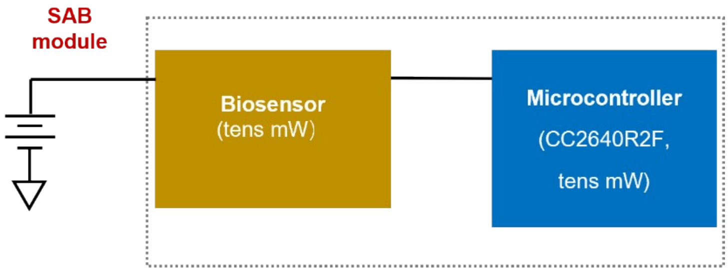

Fig. S12 Simplified block diagram of the microelectronic system. This system contains biosensor module and microcontroller module, both require tens of milliwatts of power.

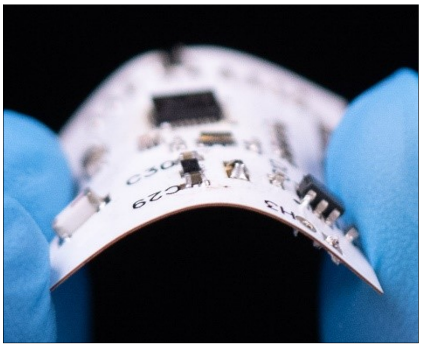

Fig. S13 Photograph of the flexible electronic module.

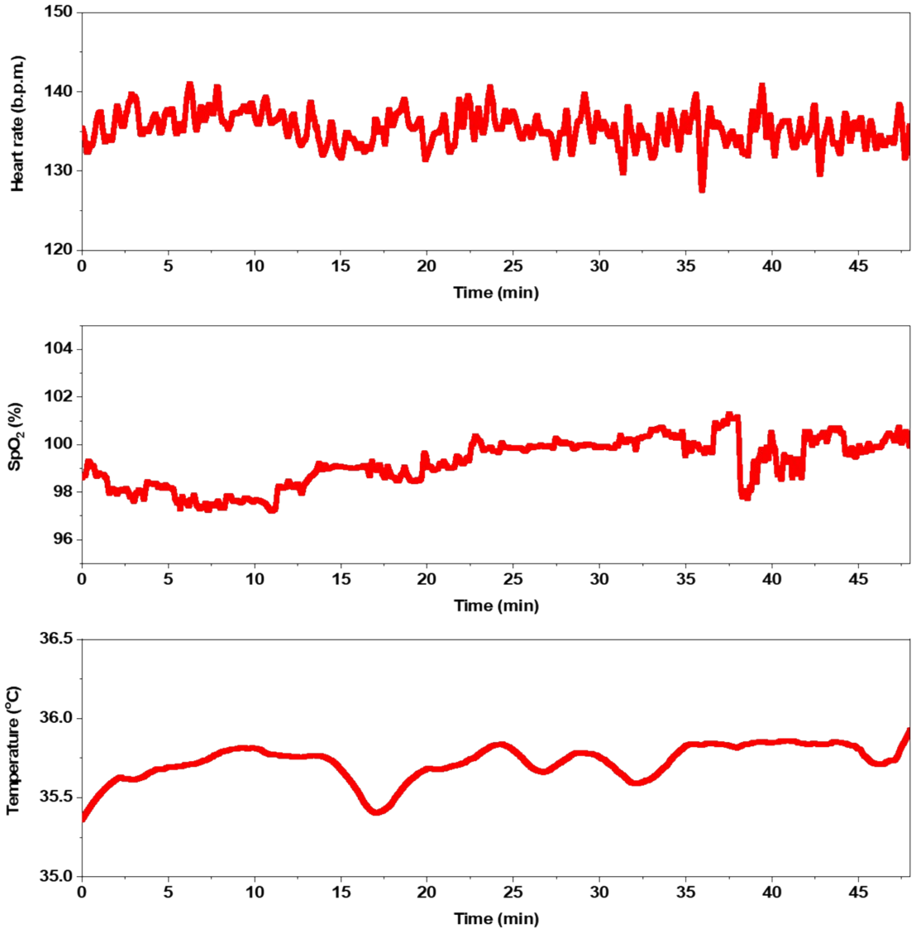

Fig. S14 The real-time physiological signals (heart rate, blood oxygen (SpO_2), and skin temperature) displayed during 48 mins jogging.